nature materials

LETTERS

PUBLISHED ONLINE: 11 JULY 2016 | DOI: 10.1038/NMAT4685

Spectroscopic evidence for a type II Weyl semimetallic state in $MoTe_2$

Lunan Huang[1], Timothy M. McCormick[2], Masayuki Ochi[3], Zhiying Zhao[4], Michi-To Suzuki[5], Ryotaro Arita[5,6], Yun Wu[1], Daixiang Mou[1], Huibo Cao[7], Jiaqiang Yan[8,9], Nandini Trivedi[2] and Adam Kaminski[1]*

In a type I Dirac or Weyl semimetal, the low-energy states are squeezed to a single point in momentum space when the chemical potential μ is tuned precisely to the Dirac/Weyl point[1-6]. Recently, a type II Weyl semimetal was predicted to exist, where the Weyl states connect hole and electron bands, separated by an indirect gap[7-10]. This leads to unusual energy states, where hole and electron pockets touch at the Weyl point. Here we present the discovery of a type II topological Weyl semimetal state in pure $MoTe_2$, where two sets of Weyl points ($W_2^{\pm}$, $W_3^{\pm}$) exist at the touching points of electron and hole pockets and are located at different binding energies above E_F. Using angle-resolved photoemission spectroscopy, modelling, density functional theory and calculations of Berry curvature, we identify the Weyl points and demonstrate that they are connected by different sets of Fermi arcs for each of the two surface terminations. We also find new surface 'track states' that form closed loops and are unique to type II Weyl semimetals. This material provides an exciting, new platform to study the properties of Weyl fermions.

It is surprising and yet exhilarating that non-interacting or quadratic Hamiltonians can continue to provide so much richness from graphene, to topological insulators and topological superconductors. This list was recently expanded by the discovery of topological Weyl semimetals (TWSs), the relatively robust three-dimensional analogues of graphene. With all three Pauli matrices involved in the Hamiltonian, perturbations only shift the position of the node in momentum space but do not open a gap.

While the massless solution to the Dirac equation[11] was first proposed by Hermann Weyl in 1929, there are no known examples of Weyl fermions in particle physics. Quantum materials' analogues have been proposed in various classes of topological Dirac[12–14] and Weyl semimetals where a pair of Dirac nodes can be separated into two Weyl points (WPs) by breaking either inversion or time-reversal invariance. The topological nature of a TWS is reflected in the Berry fluxes of opposite chirality circulating around the WPs and the presence of a Fermi arc formed between the projections of the two WPs on a surface at which the bulk is truncated.

Recently, two types of TWS have been identified: type I TWSs can be understood as the limiting point of a semiconductor with a direct bandgap that closes linearly at a set of isolated points. As a consequence, there is zero density of states if the chemical potential is tuned to the energy of the WPs. Type I TWSs have been predicted and observed in the TaAs family (TaAs, NbAs and TaP)[1–6], and also predicted to occur in pyrochlore iridates[15] and carbon allotropes[16]. Type II TWSs, on the other hand, can be understood as the limiting point of an indirect gap semiconductor that evolves into a compensated semimetal with electron and hole pockets that touch at a set of isolated points with a finite density of states at the chemical potential[17]. The two WPs connected by a Fermi arc need not occur at the same energy. $MoTe_2$, WTe_2 and $SrSi_2$ are predicted to be such a type II TWS[7–10]. The calculations based on precisely determined lattice parameters point to the presence of a quadruplet of WPs and the presence of line nodes[18]. The line nodes are very interesting topological objects that form closed contours of one-dimensional Fermi surfaces in the momentum space[19,20] that are yet to be observed experimentally. Strong spin–orbit coupling can, in principle, break them in to arcs, the presence of which was recently reported in extreme high magnetoresistive $PtSn_4$ (ref. 21). There are some signatures of a type II TWS state in the mixed compound $Mo_{0.45}W_{0.55}Te_2$ (ref. 22). Here we present the first evidence for such a state in the stoichiometric, low-scattering material $MoTe_2$.

One of the most exciting properties of a TWS is the existence of gapless Fermi arcs on the surface. A Fermi surface, defined as the locus of gapless excitations, is typically a closed contour that separates filled states from empty states at zero temperature. In view of that, a chopped up Fermi surface with the two pieces on opposite surfaces is a novel state of matter. Surface-sensitive probes such as angle-resolved photoemission spectroscopy have a decided advantage in investigating the structure of arcs, connectivity of electron and hole pockets and locations of WPs, which is the topic of our paper.

To set the stage for interpretation of the experimental results, we investigate a two-band lattice model that breaks inversion symmetry but is invariant under time-reversal symmetry. The main lessons learnt by examining this model are shown in Fig. 1 and summarized here. First, the minimum number of four Weyl nodes in this type II TWS occur at $E = 0$ at the touching point of electron and hole pockets in contrast with a type I TWS that has a zero density of states at $E = 0$. The touching of electron and hole bands in our model is similar to the touching of the electron and hole bands in the experimental data shown in Fig. 2a,b. Second, for a slab geometry, constant-energy cuts at $E = 0$ show Fermi arcs on surface

[1]Ames Laboratory, US DOE and Department of Physics and Astronomy, Iowa State University, Ames, Iowa 50011, USA. [2]Department of Physics and Center for Emergent Materials, The Ohio State University, Columbus, Ohio 43210, USA. [3]Department of Physics, Osaka University, Toyonaka, Osaka 560-0043, Japan. [4]Department of Physics and Astronomy, University of Tennessee, Knoxville, Tennessee 37996, USA. [5]RIKEN Center for Emergent Matter Science (CEMS), Wako, Saitama 351-0198, Japan. [6]JST ERATO Isobe Degenerate π-Integration Project, Advanced Institute for Materials Research (AIMR), Tohoku University, Sendai, Miyagi 980-8577, Japan. [7]Quantum Condensed Matter Division, Oak Ridge National Laboratory, Oak Ridge, Tennessee 37831, USA. [8]Materials Science and Technology Division, Oak Ridge National Laboratory, Oak Ridge, Tennessee 37831, USA. [9]Department of Materials Science and Engineering, University of Tennessee, Knoxville, Tennessee 37996, USA. *e-mail: kaminski@ameslab.gov

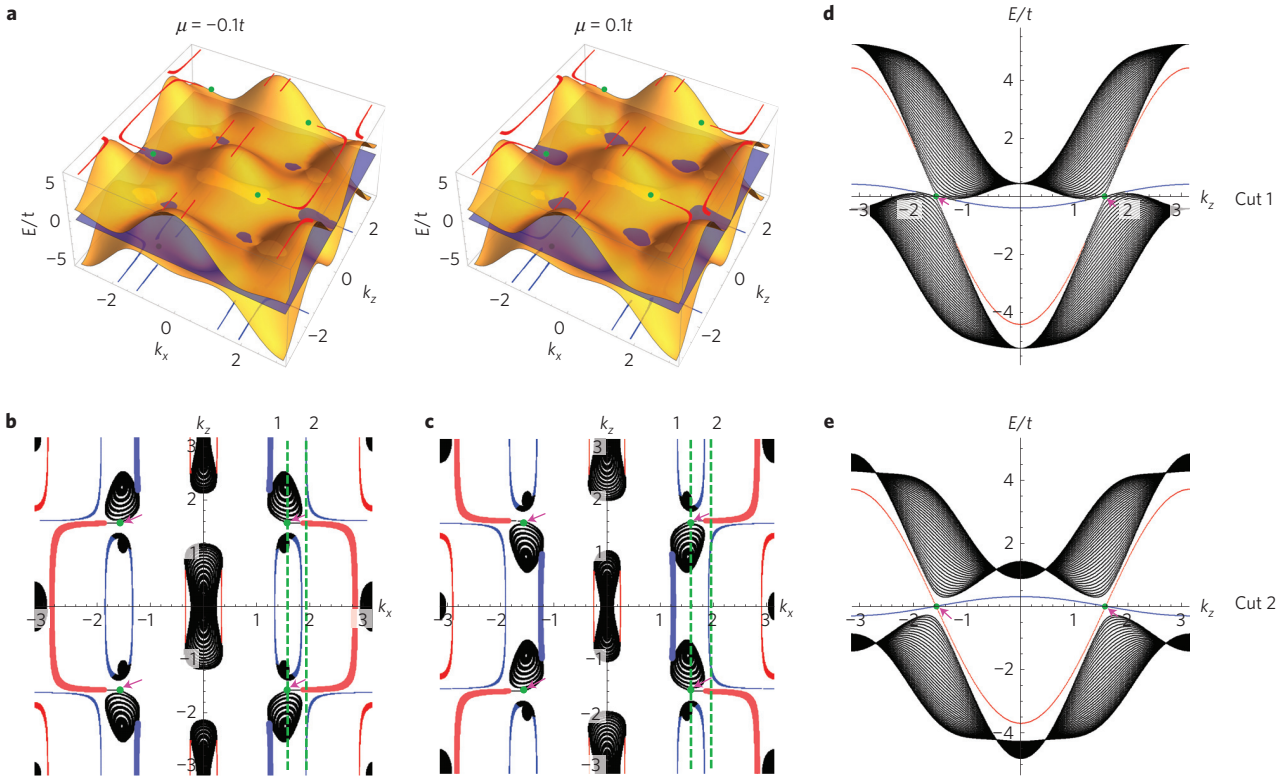

Figure 1 | A simple model of the type II Weyl semimetal described by a two-band model given by equation (2) that exhibits four Weyl nodes. a, Electronic band structure for $\mu = \pm 0.1t$ indicated by the blue translucent plane. **b**,**c**, The topological surface states and Fermi arcs on surface A (in red) and B (in blue) are calculated for a slab geometry confined along the *y*-direction. The bulk bands are shown in black. When $\mu = 0$ exactly, the electron and hole pockets touch and the arcs terminate on the node (green dot) itself. For Fermi energy below (above) the nodal energy, arcs of surface states connect the Fermi hole (electron) pockets surrounding a node rather than terminating on a node. **d**,**e**, Energy dispersion along k_z at fixed k_x as shown by the cuts in **b**,**c**. Cut 1 along $k_x = \pi/2$ shows the bulk electron and hole bands touching at the node and the merging of surface states into the bulk away from the Weyl node. Cut 2 along $k_x = 0.63\pi$ shows a gap between the bulk bands and a surface state that disperses with opposite velocities at the projections of the two WPs. The WPs are located at $(k_x, k_z) = (\pm\pi/2, \pm\pi/2)$ indicated by pink arrows pointing to green dots.

termination A and B that connect WPs of opposite chirality. In addition there are what we term 'track states' that exist on the surface and pass through the WPs but, unlike Fermi arcs, form closed loops. For $E < 0$, the projections of the WPs are within the hole pocket, and at the surface the arc states connect the two hole pockets and the track states loop around the electron pockets. The opposite is true for $E > 0$. Third, the energy dispersion clearly shows a surface state dispersing separately from the bulk bands and merging with the bulk bands close to the WP in Fig. 1d. This is corroborated by the experimental data around the Weyl nodes in Fig. 2i and Fig. 3o where the arc merges with the bulk states.

We consider the following Hamiltonian for a two-band lattice model that breaks inversion symmetry and is invariant under time-reversal:

$$\hat{H}_{\mathrm{Inv}} = \sum_{\boldsymbol{k}} \hat{c}^{\dagger}_{\boldsymbol{k}\alpha} (\hat{\mathcal{H}}(\boldsymbol{k}))_{\alpha\beta} \hat{c}_{\boldsymbol{k}\beta} \qquad (1)$$

where $\hat{c}^{(\dagger)}_{\boldsymbol{k}\alpha}$ annihilates (creates) an electron at momentum $\boldsymbol{k}$ in orbital α and

$$\begin{aligned}\hat{\mathcal{H}}(\boldsymbol{k}) = {} & \gamma(\cos(2k_x) - \cos(k_0))(\cos(k_z) - \cos(k_0))\hat{\sigma}_0 \\ & - (m(1 - \cos^2(k_z) - \cos(k_y)) + 2t_x(\cos(k_x) - \cos(k_0)))\hat{\sigma}_1 \\ & - 2t\sin(k_y)\hat{\sigma}_2 - 2t\cos(k_z)\hat{\sigma}_3 \qquad (2)\end{aligned}$$

Here $\hat{\sigma}_i$ is the ith Pauli matrix for $i = 1, 2, 3$ and $\hat{\sigma}_0$ is the 2×2 identity matrix. This model has four Weyl nodes located at $E = 0$ and $\boldsymbol{k} = (\pm k_0, 0, \pm\pi/2)$. The term in $\hat{\mathcal{H}}(\boldsymbol{k})$ proportional to $\hat{\sigma}_0$ produces a uniform shift in both energy bands. Such a momentum-dependent shift will result in a non-vanishing density of states from electron and hole pockets that touch at the Weyl node and a tilt of the Weyl nodes characteristic of a type II TWS. Henceforth, we set the parameters $m = 2t$, $t_x = t/2$, $k_0 = \pi/2$, and $\gamma = 2.4t$. The bulk band structure for this parameter choice can be seen in Fig. 1a, which shows hole and electron pockets touching at the Weyl nodes as well as pockets disconnected from the nodes. Similar Fermiology is also present in the $MoTe_2$ system and we can gain insight into this and other related materials by taking advantage of the lattice model's simplicity and tunability.

We examine the structure of the surface-state configuration by considering the model in equation (1) in a slab geometry finite in the *y*-direction with L layers but infinite in the *x*- and *z*-directions. We label the states as 'surface termination B' ('surface termination A') if they are exponentially localized at $\langle y \rangle = 1$ ($\langle y \rangle = L$). Figure 1 also shows the surface states at $\mu = \pm 0.1t$ overlaid on the bulk band structure. We show constant-energy cuts through the band structure of the slab geometry in Fig. 1b,c for $\mu = \pm 0.1t$. When $\mu < 0$, the projections of the Weyl nodes (shown by green dots) are enclosed by hole pockets. Each of these hole pockets is connected to another pocket containing a node of opposite chirality by one Fermi arc on surface A (B) shown as a thick light red (blue) line. When $\mu > 0$, the projections of the Weyl nodes are enclosed by electron pockets that are similarly connected by Fermi arcs on the surfaces. At precisely $\mu = 0$, because all of the nodes lie at $E = 0$, all Fermi arcs terminate on the nodes themselves as in a type I TWS.

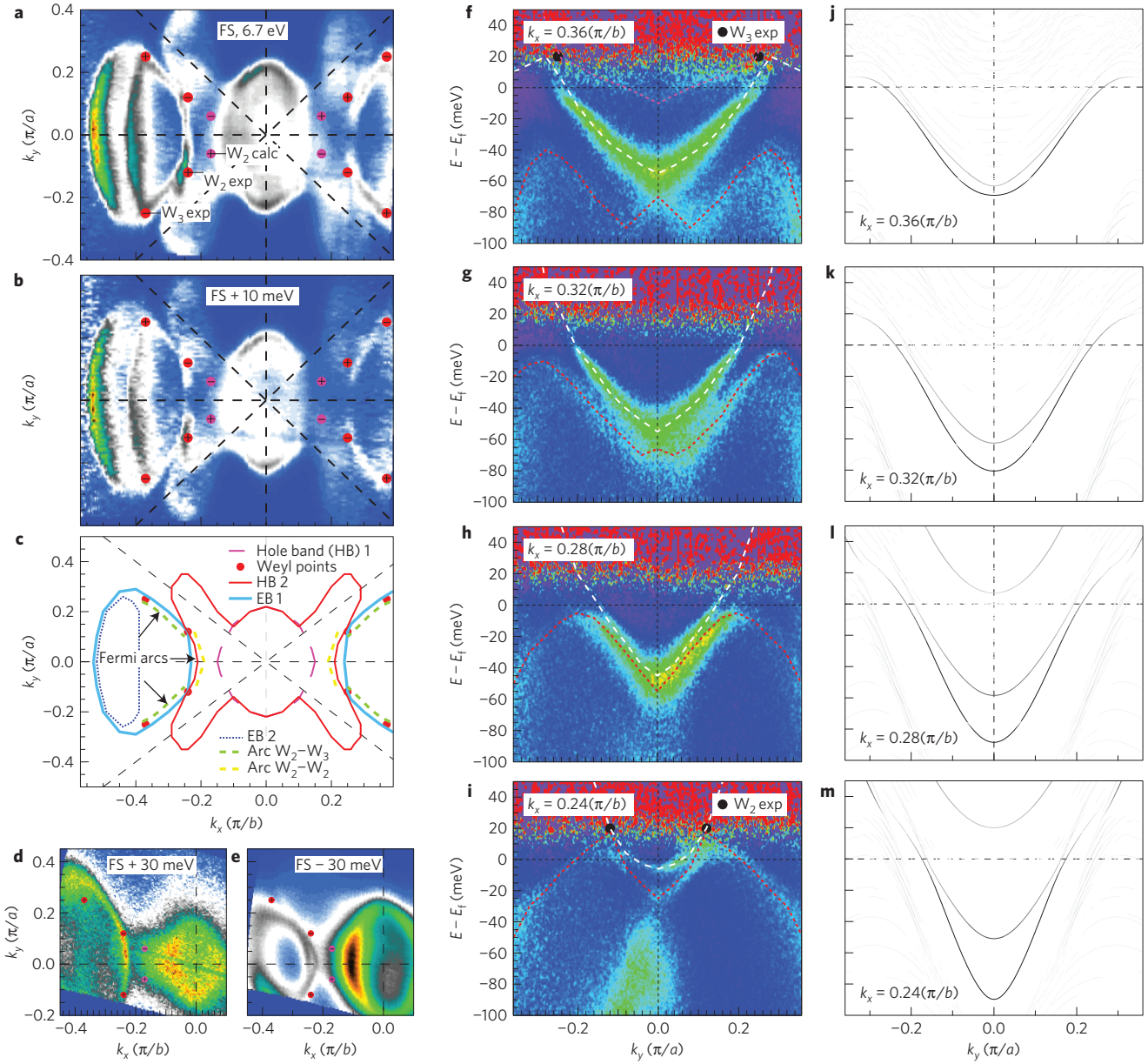

Figure 2 | Experimental Fermi surface and band structure of $MoTe_2$. a, Constant-energy intensity plot measured at E_F using 6.7 eV photons for a sample with termination A. The calculated (DFT) positions of WPs W_2 are marked as pink dots, while experimentally determined locations of W_2 and W_3 points are marked as red dots. The chiralities of WPs are marked with '+' and '−' and their locations (k_x, k_y, E) are summarized in Table 1. **b**, Same plot as in **a** but taken at 10 meV above E_F. **c**, A sketch of constant-energy contours of electron and hole bands showing the locations of WPs and Fermi arcs. **d**, Constant-energy contour measured at 30 meV above E_F using 5.9 eV photons for a sample with termination B. Positions of calculated and measured WPs are marked as above. **e**, Same surface termination and photon energy as in **d** but at 30 meV below E_F. **f–i**, Experimental band dispersion along cuts at $k_x = 0.24$, 0.28, 0.32 and 0.36 π/b. White dashed lines mark locations of the electron bands and red dashed lines mark the locations of the hole bands. **j–m**, Calculated band dispersion for a sample with termination A along $k_x = 0.24$, 0.28, 0.32 and 0.36 π/b. Bands plotted with darker lines have more surface weights. Dashed black lines in **a–d** connect the Γ point to symmetry points and to corners of the Brillouin zone.

The slab configuration energy dispersion for fixed k_x is shown in Fig. 1d,e. These cuts are shown as green dashed lines labelled cut 1 and cut 2 respectively. We can see that at the Weyl nodes, the red surface bands in Fig. 1d disappear into the bulk. As we move past the WPs in Fig. 1e, we see that these two red bands combine into a single continuous band.

$MoTe_2$ crystallizes in an orthorhombic lattice. Of the three different polymorphs, only the T_d phase (space group $Pmn2_1$, No. 31) lacks inversion symmetry and can therefore host the Weyl state[7]. Details of crystal growth and angle-resolved photoemission spectroscopy (ARPES) measurements are discussed in the Methods. The Fermi surface of $MoTe_2$ also has two 2-fold symmetry axes, along Γ–X and Γ–Y directions. The lattice constants are $a = 6.33$ Å, $b = 3.469$ Å.

We identify electron and hole bands in the spectroscopic data shown in Figs 2 and 3. The hole bands at the centre of the Brillouin zone have a 'butterfly' shape. The electron pockets shaped like ovals are located on each side of the butterfly. There are also two banana-like hole pockets partially overlapping the oval electron pockets. The configuration of these pockets can be seen at the Fermi energy in Fig. 2a and 10 meV above the Fermi energy in Fig. 2b and their electron or hole character is easily identified because hole (electron)

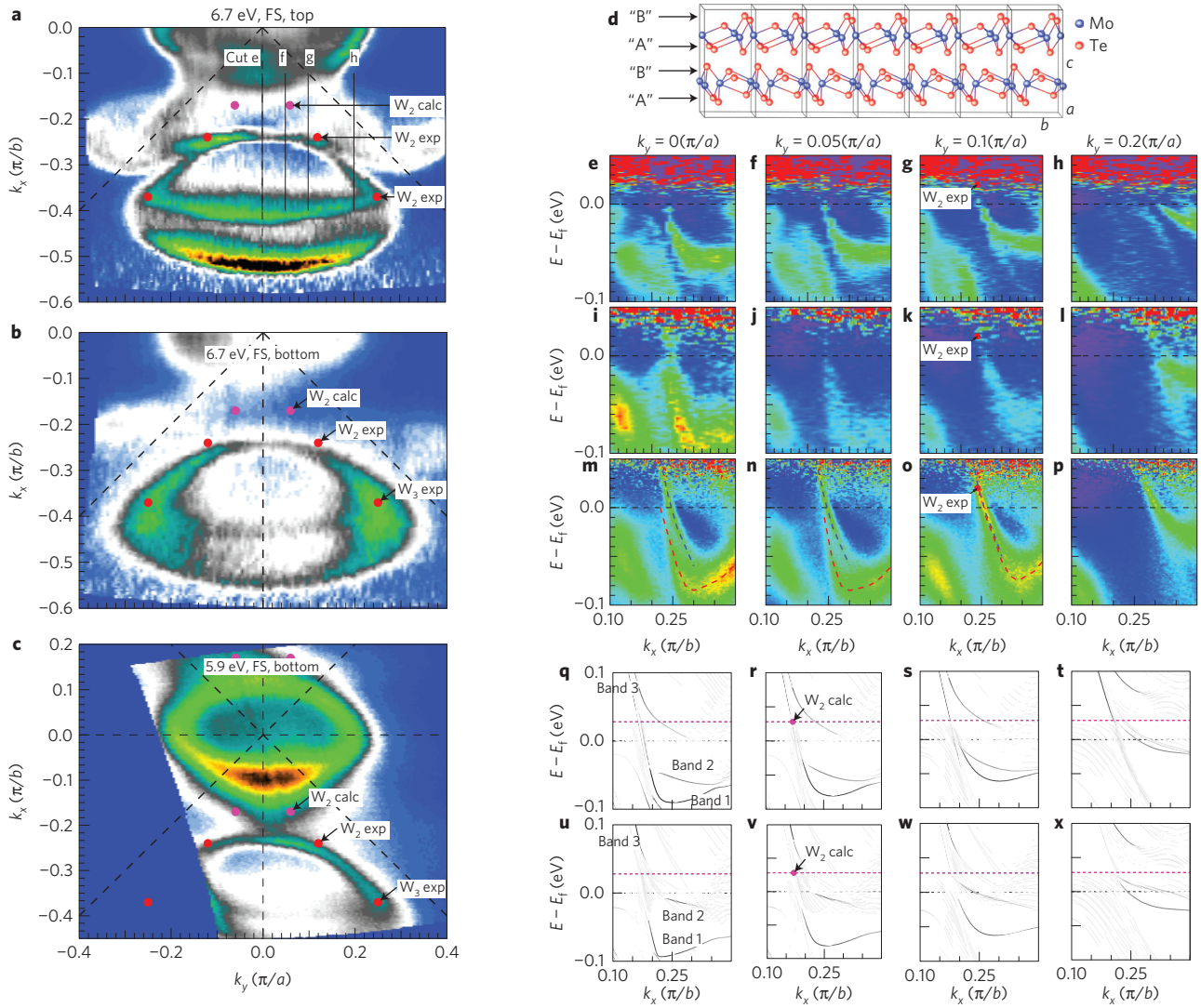

Figure 3 | Identification of WPs and Fermi arcs from experimental data. a, Constant-energy contour at E_F, measured by 6.7 eV photons for surface termination A. DFT-predicted locations for WPs W_2 and measured WPs W_2, W_3 are marked as red and pink dots, respectively. Black lines mark locations of cuts along which band dispersion data were measured. **b**, The same as in **a** except for surface termination B. **c**, The same as in **b** except for using 5.9 eV photons. Dashed black lines in **a**–**c** connect the Γ point to symmetry points and to corners of the Brillouin zone. **d**, Schematic drawing of the crystal structure of a single unit cell layer with two different possible surface terminations 'A' and 'B' marked by arrows. **e**–**h**, Energy dispersion for surface termination A along $k_y = 0$, 0.05, 0.10 and 0.20 π/a using 6.7 eV photons. The projections of WPs W_2 are marked as dots. **i**–**l**, The same as in **e**–**h** except for surface termination B. **m**–**p**, The same as in **i**–**l** except for using 5.9 eV photons. The blue dashed line marks the dispersion of the electron band and the red dashed line marks the dispersion of the hole band. **q**–**t**, Calculated band dispersion for surface termination A along cuts at $k_y = 0$, 0.05, 0.10 and 0.20 π/a. The positions of W_2 are marked similarly as above. The pink dashed line marks the calculated energy of the W_2. **u**–**x**, The same as in **q**–**t** except for surface termination B. Bands plotted with darker lines have more surface weights.

pockets shrink (expand) with increasing energy. A simplified sketch of constant-energy contours of electron and hole bands is shown in Fig. 2c.

The central hole pocket touches the electron pockets at four WPs shown as red dots in Fig. 2a–c that we label as W_2. The outer banana-shaped hole pockets also touch the oval electron pockets at two other WPs labelled as W_3. At surface termination A (Fig. 2b), those two types of WP are connected by topological arcs seen as white–grey high-intensity areas. For this surface termination there is no strong evidence for arcs connecting positive and negative chirality W_2 nor positive and negative chirality W_3 points. The situation for surface termination B is more complicated as shown in Fig. 2d. There seems to be a sharp contour connecting both sets of W_2 and W_3 points. Most likely this is a track state discussed above. The examination of the constant-energy plot at energy of 30 meV below E_F (Fig. 2e) reveals that there are actually two bands present. In addition to the track state, there is also an arc present that connects positive and negative chirality W_2 points. Although the present data do not allow us to definitely demonstrate a connection between positive and negative chirality W_3 points, we can deduce that they are likely to be connected, so the arcs on surface A between W_2–W_3 together with arcs on surface B W_2^+–W_2^- and W_3^+–W_3^- form a closed loop when connected via the bulk of the sample.

We now examine the locations of the WPs in the band dispersion. In Fig. 2f–i we plot the band dispersion along the k_y cut for selected values of k_x. At $k_y = 0.36\pi/b$ (Fig. 2f) two bands are clearly visible: an M-shaped band at higher binding energy and a U-shaped band at slightly lower binding energy. Both bands appear connected at zero momentum with Dirac-like structure. As we move towards the zone centre, both bands move to lower binding energy and their

Table 1 | The locations (k_x,$k_{y,E}$) of the WPs from DFT (calculated using experimental crystal structure parameters) and ARPES.

	k_x (π/b)	k_y (π/a)	E (meV)
W_2 DFT	±0.17	±0.06	28
W_2 Exp	±0.24	±0.12	20
W_3 Exp	±0.37	±0.25	30

energy separation decreases. In Fig. 2h, the tips of the M-shaped band (red dotted line) touch the E_F and form parts of the butterfly hole pockets. As these tips move above E_F, they merge with the wings of the U-shaped electron band (white dotted line) forming two WPs approximately 20 meV above E_F marked by black dots. At each side of the symmetry line, they form two tilted cones characteristic of a type II Weyl node. The $MoTe_2$ samples cleave between two adjacent Te layers (see Fig. 3d). The crystal structure of the T_d phase, which hosts the Weyl state, breaks the inversion symmetry and there are two $MoTe_2$ layers per unit cell. This gives rise to two chemically similar, but structurally different cleaving planes 'A' and 'B', as shown in Fig. 3d. The electronic structure of each termination is expected to be slightly different due to the different length of the Mo–Te bonds. The data along the k_x direction are shown in Fig. 3e–p along with results of calculations (Fig. 3q–x) for the two surface terminations. The surface termination A is characterized by lower binding energy of the electron pocket in Fig. 3e–h, when compared with the data from surface termination B shown in Fig. 3i–p. The data in Fig. 3m–p best illustrate the formation of the W_2 points. In Fig. 3m, the hole band is marked with a red dashed line, while the electron band is marked with a blue dashed line. As we move away from the symmetry line, the separation between those bands becomes smaller and they merge at a point located ~20 meV above E_F marked by a red dot in panel Fig. 3o. For higher values of k_y momentum they separate again as seen in panel Fig. 3p. The density functional theory (DFT) calculation also demonstrates the energy difference of the band locations for the two terminations and formation of the W_2 WP that agrees with experiment on a qualitative level. The details of the DFT calculations are provided in the Methods.

The momentum location of the experimentally determined WPs is different from DFT predictions (marked as pink dots in 2a,b) most likely due to high sensitivity of the band calculation to structural parameters. Table 1 summarizes the positions of WPs determined from experiment and DFT. Despite the discrepancy between the predicted locations of the Weyl nodes from DFT and where they are located experimentally, in each case they are at the touching points of the electron and hole bands. In the $k_y = 0$ cuts shown in Fig. 3e,l,m,q,u, band 1 is connected to bulk states below the Fermi level, while band 3 dips down and goes into bulk just before it reaches the WP. As we increase k_y, band 1 and band 3 merge together. In

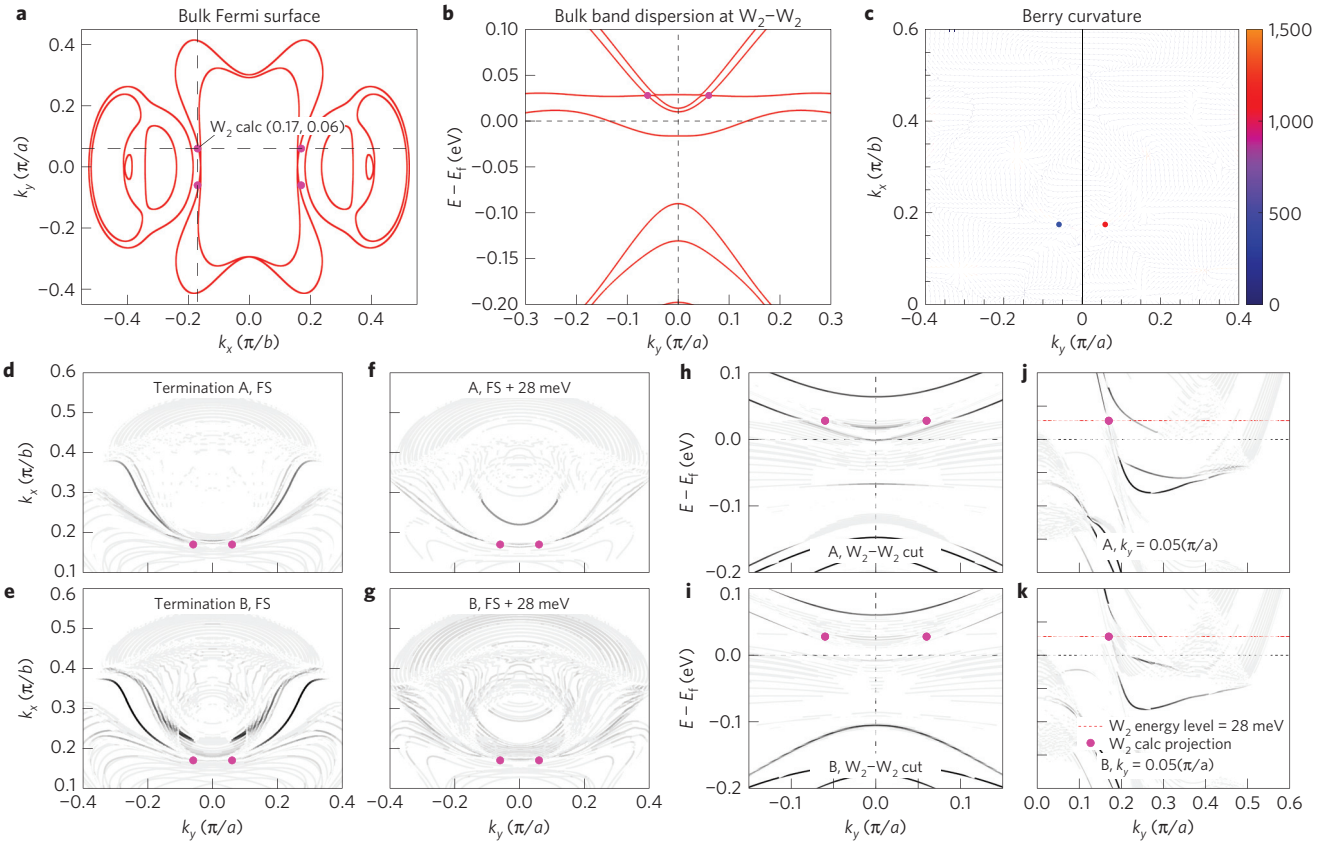

Figure 4 | Results of DFT calculations. a, Calculated bulk Fermi surface of $MoTe_2$ for $k_z = 0.6\pi/c$ and projections of W_2 $(k_x, k_y) = (\pm 0.17\pi/b, \pm 0.06\pi/a)$ are marked with pink dots. **b**, Bulk band dispersion along the W_2-W_2 direction (the vertical dashed line in **a**). DFT-predicted positions of W_2 $(k_y, E) = (\pm 0.06\pi/a, 0.028\,\text{eV})$ are marked. **c**, The dominant contribution for the divergence of the Berry curvature $(\Omega^{DD}_{n,yz}, \Omega^{DD}_{n,zx})$ for the $n = N + 1$th band, where N is the number of electrons in the unit cell with $k_z = 0$. Red and blue indicate different chiralities of the two WPs. **d**–**g**, Calculated constant-energy contours of $MoTe_2$. Darker bands are surface bands and lighter bands are bulk bands. **d**,**e** are at the Fermi level for surface termination A and B. **f**,**g** are at the Fermi level + 28 meV of surface termination A and B, respectively. **h**–**i**, Surface band dispersions of termination A and B along the W_2-W_2 direction. **j**–**k**, Surface band dispersions of termination A and B along the $k_y = 0.05\pi/a$ direction, which is very close to the k_y position of W_2 $(0.06\pi/a)$. Positions of calculated WPs W_2 are marked and darker bands have more surface weight in **d**–**k**.

the $k_y = 0.1\pi/a$ cuts, the two bands merge into one band that goes through the position of the projection of W_2. This behaviour is exactly the behaviour predicted in Fig. 1d,e.

Figure 4 shows the DFT calculation of the band structure of $MoTe_2$. In Fig. 4a we plot the bulk Fermi surface for $k_z = 0.6\pi/c$ and positions of four WPs calculated using structural parameters determined experimentally from X-ray scattering data. The shapes of the outermost electron and hole bands are very similar to our experimental result in Fig. 2b. The pink dots are projections of the calculated WPs on the $k_z = 0$ plane from energy +28 meV above the Fermi level; thus, the electron band is not touching the two WP projections. The surface-weighted constant-energy contours are shown in 4d–g. Figure 4d,e are at Fermi surfaces of termination A and B, while 4f,g are at Fermi level +28 meV, the DFT-predicted energy of W_2. In the calculations, W_2 is not directly connected to another W_2 by surface states on the Fermi surface of termination A calculation while they are connected by weak and short surface states in termination B calculation. However, the W_2 points are connected by bulk electron bands in termination A. This is consistent with our experimental results shown in Fig. 2a–e. Figure 4b shows the bulk band dispersion in the W_2–W_2 direction, as indicated by the vertical dashed line in 4a. The two W_2 points from DFT are right at the touching points of one hole band and one electron band. Figure 4h,i shows termination A and B surface band dispersions along the same direction as in Fig. 4b. The surface bands are to connect bulk states near the positions of the WPs. Figure 4j,k shows termination A and B surface band dispersions along the $k_y = 0.05\pi/a$ direction, as the horizontal dashed line shown in 4a. We also calculated the Berry curvature on the Fermi surface. The bright points in Fig. 4c are possible singular points of the Berry curvature and DFT-calculated W_2 points are marked in red and blue, indicating different chiralities of the WPs. The summary of energy and momentum locations of WPs based on calculations and experiment is provided in Table 1. It should be noted that WPs are not protected by crystal symmetry and their calculated locations are very sensitive to structural parameters as discussed in the Methods.

Our results demonstrate that the $MoTe_2$ hosts an exotic type II Weyl semimetallic state. We identified the presence of Fermi arcs, WPs and novel track surface states in our ARPES data. This material is therefore an excellent playground to explore the fascinating physics of Weyl fermions. We anticipate that these results will be of interest to the general physics community due to the relevance for high-energy particle theory and also for more applied materials field, because the presence of the WPs and Fermi arcs may lead to interesting and potentially useful transport properties.

Methods

Methods and any associated references are available in the online version of the paper.

Received 22 March 2016; accepted 31 May 2016; published online 11 July 2016

References

1. Weng, H., Fang, C., Fang, Z., Bernevig, B. A. & Dai, X. Weyl semimetal phase in noncentrosymmetric transition-metal monophosphides. *Phys. Rev. X* **5,** 011029 (2015).
2. Xu, S.-Y. *et al*. Discovery of a Weyl fermion semimetal and topological Fermi arcs. *Science* **349,** 613–617 (2015).
3. Yang, L. X. *et al*. Weyl semimetal phase in the non-centrosymmetric compound TaAs. *Nature Phys.* **11,** 728–733 (2015).
4. Lv, B. Q. *et al*. Observation of Weyl nodes in TaAs. *Nature Phys.* **11,** 724–728 (2015).
5. Xu, S.-Y. *et al*. Discovery of a Weyl fermion state with Fermi arcs in niobium arsenide. *Nature Phys.* **11,** 748–754 (2015).
6. Liu, Z. K. *et al*. Evolution of the Fermi surface of Weyl semimetals in the transition metal pnictide family. *Nature Mater.* **15,** 27–32 (2015).
7. Sun, Y., Wu, S.-C., Ali, M. N., Felser, C. & Yan, B. Prediction of Weyl semimetal in orthorhombic $MoTe_2$. *Phys. Rev. B* **92,** 161107 (2015).
8. Soluyanov, A. A. *et al*. Type-II Weyl semimetals. *Nature* **527,** 495–498 (2015).
9. Lv, B. Q. *et al*. Experimental discovery of Weyl semimetal TaAs. *Phys. Rev. X* **5,** 031013 (2015).
10. Huang, S.-M. *et al*. New type of Weyl semimetal with quadratic double Weyl fermions. *Proc. Natl Acad. Sci. USA* **113,** 1180–1185 (2016).
11. Weyl, H. Gravitation and the electron. *Proc. Natl Acad. Sci. USA* **15,** 323–334 (1929).
12. Hsieh, D. *et al*. A topological Dirac insulator in a quantum spin Hall phase. *Nature* **452,** 970–974 (2008).
13. Burkov, A. A. & Balents, L. Weyl semimetal in a topological insulator multilayer. *Phys. Rev. Lett.* **107,** 127205 (2011).
14. Liu, Z. K. *et al*. Discovery of a three-dimensional topological Dirac semimetal, Na_3Bi. *Science* **343,** 864–867 (2014).
15. Wan, X., Turner, A. M., Vishwanath, A. & Savrasov, S. Y. Topological semimetal and Fermi-arc surface states in the electronic structure of pyrochlore iridates. *Phys. Rev. B* **83,** 1–9 (2011).
16. Chen, Y. *et al*. Nanostructured carbon allotropes with Weyl-like loops and points. *Nano Lett.* **15,** 6974–6978 (2015).
17. Xu, Y., Zhang, F. & Zhang, C. Structured Weyl points in spin-orbit coupled fermionic superfluids. *Phys. Rev. Lett.* **115,** 265304 (2015).
18. Wang, Z. *et al*. $MoTe_2$: Weyl and line node topological metal. Preprint at http://arxiv.org/1511.07440 (2015).
19. Burkov, A. A., Hook, M. D. & Balents, L. Topological nodal semimetals. *Phys. Rev. B* **84,** 235126 (2011).
20. Heikkil, T. & Volovik, G. Dimensional crossover in topological matter: evolution of the multiple Dirac point in the layered system to the flat band on the surface. *JETP Lett.* **93,** 59–65 (2011).
21. Wu, Y. *et al*. Dirac node arcs in $PtSn_4$. *Nature Phys.* **12,** 667–671 (2016).
22. Belopolski, I. *et al*. Unoccupied electronic structure and signatures of topological Fermi arcs in the Weyl semimetal candidate $Mo_xW_{1-x}Te_2$. Preprint at http://arxiv.org/1512.09099 (2015).
23. Canfield, P. C., Kong, T., Kaluarachchi, U. S. & Jo, N. H. Use of frit-disc crucibles for routine and exploratory solution growth of single crystalline samples. *Phil. Mag.* **96,** 84–92 (2016).
24. Jiang, R. *et al*. Tunable vacuum ultraviolet laser based spectrometer for angle resolved photoemission spectroscopy. *Rev. Sci. Instrum.* **85,** 033902 (2014).
25. Perdew, J. P., Burke, K. & Ernzerhof, M. Generalized gradient approximation made simple. *Phys. Rev. Lett.* **77,** 3865–3868 (1996).
26. Blaha, P., Schwarz, K., Madsen, G. K. H., Kvasnicka, D. & Luitz, J. *WIEN2K, An Augmented Plane Wave + Local Orbitals Program for Calculating Crystal Properties* (Karlheinz Schwarz, Techn. Universität Wien, 2001).
27. Marzari, N. & Vanderbilt, D. Maximally localized generalized Wannier functions for composite energy bands. *Phys. Rev. B* **56,** 12847–12865 (1997).
28. Souza, I., Marzari, N. & Vanderbilt, D. Maximally localized Wannier functions for entangled energy bands. *Phys. Rev. B* **65,** 035109 (2001).
29. Mostofi, A. A. *et al*. Wannier90: a tool for obtaining maximally-localized Wannier functions. *Comput. Phys. Commun.* **178,** 685–699 (2008).
30. Wang, X., Yates, J. R., Souza, I. & Vanderbilt, D. *Ab initio* calculation of the anomalous Hall conductivity by Wannier interpolation. *Phys. Rev. B* **74,** 195118 (2006).

Acknowledgements

The work at Ames Laboratory was supported by the US Department of Energy, Office of Science, Basic Energy Sciences, Materials Science and Engineering Division (ARPES measurements). Ames Laboratory is operated for the US Department of Energy by Iowa State University under contract No. DE-AC02-07CH11358. Data analysis, theory and modelling was supported by the Center for Emergent Materials, an NSF MRSEC, under grant DMR-1420451. T.M.M. acknowledges funding from NSF-DMR-1309461 and would like to thank the 2015 Princeton Summer School for Condensed Matter Physics for their hospitality. N.T. acknowledges partial support by a grant from the Simons Foundation (no. 343227). Work at ORNL (sample growth) was supported by the US Department of Energy, Office of Science, Basic Energy Sciences, Scientific User Facilities Division (H.C.), and Materials Science and Engineering Division (J.Y.).

Author contributions

N.T. and T.M.M. provided theoretical modelling and interpretation. J.Y. and Z.Z. grew the samples. M.O., M.-T.S. and R.A. performed DFT and Berry phase calculations. H.C. performed crystal structure determination. L.H., Y.W. and D.M. performed ARPES measurements and support. L.H. analysed ARPES data. The manuscript was drafted by L.H., T.M.M., N.T. and A.K. All authors discussed and commented on the manuscript.

Additional information

Reprints and permissions information is available online at www.nature.com/reprints. Correspondence and requests for materials should be addressed to N.T. or A.K.

Competing financial interests

The authors declare no competing financial interests.

Methods

Sample growth. $MoTe_2$ single crystals were grown out of a Te-rich binary melt using a Canfield crucible set (CCS)[23]. Mo and Te shots in a ratio of 1:9 were loaded into a 5 ml CCS and sealed in a quartz tube under vacuum. The quartz ampoule was heated to 1,000 °C and kept at this temperature for a week. $MoTe_2$ single crystals were isolated from Te flux by centrifuging. Different from most flux growths in which crystals precipitate while cooling from the homogenizing temperature, our growth was performed at a fixed temperature. Single crystals grown in this strategy have an RRR 500 and MR 40,000% at 2 K in an applied magnetic field of 100 kOe.

Measurements. ARPES measurements were carried out using a laboratory-based system consisting of a Scienta R8000 electron analyser and a tunable vacuum ultraviolet laser light source[24]. The data were acquired using a tunable vacuum ultraviolet laser ARPES system, consisting of a Scienta R8000 electron analyser, picosecond Ti:sapphire oscillator and fourth harmonic generator. Angular resolution was set at ∼0.05° and 0.5° (0.005 $Å^{-1}$ and 0.05 $Å^{-1}$) along and perpendicular to the direction of the analyser slit (and thus cut in the momentum space), respectively; and energy resolution was set at 1 meV. The size of the photon beam on the sample was ∼30 μm. Samples were cleaved *in situ* at a base pressure lower than 1×10^{-10} torr. Samples were cooled using a closed-cycle He refrigerator and the sample temperature was measured using a silicon-diode sensor mounted on the sample holder. The energy corresponding to the chemical potential was determined from the Fermi edge of a polycrystalline Au reference in electrical contact with the sample.

DFT calculations. We first performed first-principles band structure calculations for bulk using the Perdew–Burke–Ernzerhof parametrization of the generalized gradient approximation[25] and the full-potential (linearized) augmented plane wave plus local orbitals (FP−(L)APW+lo) method including the spin–orbit coupling as implemented in the wien2k code[26]. We employed the crystal structure determined by our experiment. The muffin-tin radii for Mo and Te atoms, r_{Mo} and r_{Te}, were set to 2.50 and 2.33 a.u., respectively. The maximum modulus for the reciprocal lattice vectors K_{max} was chosen so that $r_{Te}K_{max} = 8.00$. Next we constructed a tight-binding model consisting of Mo 4*d* and Te 5*p* orbitals, the parameters in which were extracted from the calculated band structure using the Wannier functions[27–29] without the maximal localization procedure. Then we made the slab tight-binding model of finite layers, and obtained the band structures and Fermi surfaces. The Mo and Te states on the top or bottom two layers, that is, the unit cells of surface A or B, are emphasized in each figure. To identify the position of the WPs, we also calculated the Berry curvature for bulk structure using the tight-binding model obtained above. The dominant contribution for the divergence of the Berry curvature ($\Omega^{DD}_{n,yz}, \Omega^{DD}_{n,zx}$) presented in equation (30) of ref. 30 was calculated and shown in the figure. Since WPs are not protected by crystal symmetry, their calculated locations are very sensitive to structural parameters. To demonstrate this, we calculated the positions of the WPs using the structure where all Te atoms are shifted with the crystal coordinate $z = \pm 0.005c$ so that the Mo–Te distance becomes longer in the z-direction. In such a case, the location of the W_2 point changes from momentum $(0.17\pi/b, 0.06\pi/a)$ and energy of $E_F + 28$ meV to $(0.19\pi/b, 0.04\pi/a)$ and energy of $E_F + 48$ meV. In addition, the calculation error arising from the generalized gradient approximation is also likely to be contributing to the difference between W_2 DFT and W_2 Exp results.